Acta Materialia 215 (2021) 117038

Contents lists available at ScienceDirect

Acta Materialia

journal homepage: www.elsevier.com/locate/actamat

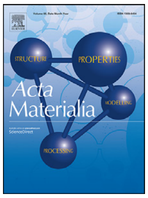

Full length article

Phase diagrams, superdomains, and superdomain walls in $K_xNa_{1-x}NbO_3$ epitaxial thin films

Meng-Jun Zhou[a,1,*], Bo Wang[b,1,*], Adriana Ladera[b,c], Laura Bogula[d], Han-Xing Liu[a], Long-Qing Chen[b], Ce-Wen Nan[e]

[a] *State Key Laboratory of Advanced Technology for Materials Synthesis and Processing, Center of Smart Materials and Devices, School Material Science and Engineering, Wuhan University of Technology, Wuhan 430070, China*
[b] *Department of Materials Science and Engineering and Materials Research Institute, The Pennsylvania State University, University Park, Pennsylvania 16802, United States*
[c] *Department of Computer Science and Engineering, University of South Florida, Tampa, Florida 33620, United States*
[d] *Leibniz-Institut für Kristallzüchtung, Max-Born-Str. 2, Berlin 12489, Germany*
[e] *School of Materials Science and Engineering, State Key Lab of New Ceramics and Fine Processing, Tsinghua University, Beijing 100084, China*

ARTICLE INFO

Article history:
Received 17 March 2021
Revised 23 May 2021
Accepted 26 May 2021
Available online 7 June 2021

Keywords:
Ferroelectrics thin films
Domain structures
Superdomain
Phase diagram
Phase-field simulation

ABSTRACT

Domains and domain walls play a critical role in determining the functional properties of ferroelectric thin films for various applications. Understanding the formation and structures of the domains and domain walls is of vital importance to manipulating their configurations and exploring their dynamics. When domains assemble into hierarchical structures, the superdomains and superdomain walls emerge, which exhibits exotic morphology and may lead to distinct new behaviors. Here, taking the $K_{0.5}Na_{0.5}NbO_3$ thin films as a model system, we establish the misfit strain-misfit strain phase diagram at different temperatures and study the formation condition, morphological features, and polarization configurations of two types of superdomain structures by using phase-field simulations, which compare well with prior experiments. We show how the superdomain structures can be viewed as superposition of two sets of polytwin structures along well-defined planes. Several types of superdomain walls are identified, which possess different energies and finite thickness in analogy to conventional domain walls. We also show that some superdomain walls can be anomalously wide and electrically conductive. This work can generate new interests in exploring the structures and functionalities of superdomain and superdomain walls in ferroelectric thin films, which can potentially be utilized for next-generation electronic devices.

1. Introduction

Domain structure has been one of the core topics in the study of ferroelectric and related materials for decades [1]. These mesoscale features can span across several length scales from nanometers to millimeters and significantly impact the macroscopic properties of the ferroelectric materials, including the piezoelectric coefficients [2], coercive fields [3,4], switching dynamics [5], optical properties [6], etc. Many functional applications of ferroelectric materials, such as piezoelectric transducers [7], nonvolatile memories [8], negative-capacitance electronics [9], and nonlinear optical devices [10], rely on the creation and control of specific domain structures. Therefore, it is of critical importance to understanding the equilibrium structure of ferroelectric domains and their dynamic evolution under various external stimuli.

In ferroelectric epitaxial thin films, the reduced dimension and modified boundary conditions result in thermodynamically stable nanosized domains separated by high-density domain walls. For perovskite oxide thin films, typical polytwin structures consisting of two alternating domain variants include a/c domains [11], a_1/a_2 [12] domains in tetragonal thin films (such as $BaTiO_3$ and $PbTiO_3$), and the 71° [13,14], 109° [13], and 180° domains [15] in rhombohedral thin films (such as $BiFeO_3$). More complicated domain structures may form through a combination of these elementary polytwins [16], which can be achieved by tuning the misfit strains [17–21], film orientations [22–25], and film thicknesses [18]. These self-organized polytwins often exhibit hierarchical organization and demonstrate dynamic behaviors that mimic a monodomain state at a larger length scale and hence are termed as the “superdomains.” For example, the superdomains can be switched as a whole by electrical [19,26] and mechanical stimuli [27] through the forma-

---

* Corresponding authors.
E-mail addresses: zhoumj@whut.edu.cn (M.-J. Zhou), bzw133@psu.edu (B. Wang).
[1] These authors contributed equally to this work.

https://doi.org/10.1016/j.actamat.2021.117038

tion and propagation of superdomain boundaries [26], similar to the reversal of a monodomain through the nucleation and growth of the reversed domain variant [28,29]. The structure and dynamics of these superdomains and superdomain boundaries have aroused increasing interests [30] due to their intriguing behaviors such as periodic doubling [31], unconventional relaxation [32], and super-switching [19] as well as their potential for novel electronics applications [33]. Notably, the term ‘superdomain’ may have been used to refer to distinct types of domain structures in different contexts. Here, we adopt a generic definition of ‘superdomain’ as the domain structure consisting of two or more bundles of twin polydomains that are separated by a macroscopically well-defined boundary, i.e., the superdomain boundary. In this sense, the flux-closure quadrants of a_1/a_2 domains [19,20,30], the antiparallel bundles of a/c domains [21,26], the three-fold symmetrical domain bundles in (111)-oriented films [22–25], and the mixture of a/c- and a_1/a_2-type domains [18,27], can all be regarded as ‘superdomains’.

Most of the superdomains mentioned above are found in thin films of tetragonal or rhombohedral ferroelectric perovskite oxides [34]. Theoretical studies on the twin polydomain structure of ferroelectrics have been established, also with a focus on the tetragonal or rhombohedral phases [35–39]. In contrast, the lower-symmetric orthorhombic phase, such as that of $K_xNa_{1-x}NbO_3$ ($x \geq 0.5$) [40], has more energetically degenerate domain variants and corresponding domain walls, which is likely to form other types of superdomain structures. For example, recent experiments have observed hierarchical ferroelectric domains with stripe-like or herringbone-like patterns in $K_xNa_{1-x}NbO_3$ epitaxial thin films grown on $(110)_O$-oriented scandate substrates [41–43]. The stripe-like superdomains have been found in $K_xNa_{1-x}NbO_3$ ($0.54 \leq x \leq 0.77$) films grown on the substrates that impart biaxial compressive misfit strains [41] while the herringbone-like ones emerge in $K_xNa_{1-x}NbO_3$ films ($0.80 \leq x \leq 0.95$) grown on $NdScO_3$ [42] substrate that imposes highly anisotropic misfit strains to the film. The herringbone-like superdomains can also undergo a structural phase transition into a high-temperature orthorhombic phase which exhibits another stripe-like superdomain pattern [44,45]. Since the in-plane misfit strains imparted by these substrates are anisotropic in general, the bulk orthorhombic symmetry (Amm2) is reduced to the monoclinic symmetry (Pm) in the film, which further complicates the morphological features of the domains and domain walls. In fact, it has been shown that the domain wall orientation in the herringbone-like domains varies with respect to the chemical composition [46]. Despite these efforts, it is still challenging to realize and understand the three-dimensional arrangement of the superdomains solely from experimental characterization [47]. The configuration of ferroelectric polarization in the superdomains, particularly near the superdomain boundaries, is not well understood.

From the perspective of applications, $K_{0.5}Na_{0.5}NbO_3$(KNN)-based ceramics and bulk crystals [48–55] have been regarded as one of the most promising lead-free piezoelectric materials [56] that exhibits comparable piezoelectric performance with PZT [57] and thus have been extensively investigated [49,51,55]. There is also growing interest to explore the ferroelectric, piezoelectric, and other functional properties of $K_xNa_{1-x}NbO_3$-based epitaxial thin films [47,58–64]. For example, enhanced piezoelectric responses have been shown at elevated temperatures close to a phase transition from the M_C phase to the M_A phase in doped KNN epitaxial thin films [59,65]. Very recently, ultrahigh dielectric tunability has been shown in KNN films with the tetragonal phase [66]. In this sense, a concrete understanding of the phase stability over a wide range of misfit strains and temperatures and the corresponding domain configurations is indispensable.

Although there have been a few theoretical studies on the phase stability and domain structures of KNN thin films at different misfit strain states [45,67], they are either based on a single-domain assumption at room temperature [67,68] or have not fully considered the anisotropy nature of the misfit strains for KNN thin films grown on $(110)_O$ scandate substrates [45]. Recently, Wang et al. studied the misfit strain-misfit strain phase diagrams based on the strain phase separation theory for KNN of various compositions and identified two simple polytwin structures [69]. However, it remains unknown how these polytwins can be assembled to form the superdomains with herringbone-like and stripe-like patterns and how the local polarization is arranged near the superdomain boundaries.

In this work, we present a systematic theoretical investigation on the formation conditions and equilibrium structures of the superdomains in KNN epitaxial thin films based on phase-field simulations. We first establish the misfit strain-misfit strain phase diagrams at different temperatures by high-throughput phase-field simulations and identify the formation conditions of the herringbone-like and stripe-like superdomains. To understand how the superdomains are related to the two sets of polytwin, we enumerate all possible combinations from the symmetry consideration and discuss the most likely configurations based on energy analysis and comparison with experiments. We found subtle features in the local morphology and polarization distribution associated with the superdomain walls. It is further identified that different types of superdomain boundaries may host distinct bound charges, implying the presence of conductive superdomain boundaries, which could bring new functional modalities for domain wall-based nanoelectronics.

2. Method

We adopt the phase-field model of ferroelectric thin films described in Refs. [70–72]. In the phase-field model, the spontaneous polarization $\boldsymbol{P} = (P_1, P_2, P_3)$ serves as the order parameter, the evolution of which is governed by the time-dependent Ginzburg-Landau (TDGL) equation

$$\frac{\partial P_i(x,t)}{\partial t} = -L\frac{\delta F}{\delta P_i(x,t)},\quad (i = 1,2,3) \tag{1}$$

where F and L represent the total free energy of the system and the kinetic coefficient, respectively. The total free energy F for the film consists of Landau energy f_{bulk}, gradient energy f_{wall}, electric energy f_{elec}, and elastic energy f_{elas}, i.e.,

$$F = \int_V \left[f_{\text{bulk}}(P_i) + f_{\text{wall}}(P_{i,j}) + f_{\text{elec}}(P_i, E_i) + f_{\text{elas}}(P_i, \varepsilon_{ij})\right]dV. \tag{2}$$

The detailed expressions for f_{bulk}, f_{wall}, f_{elec} and f_{elas} are described in literatures [71–73]. The temporal iteration of the TDGL eqaution is achieved by the semi-implicit Fourier spectral method which is implemented in the phase-field package μ-Pro® [74]. At each time step, the electrostatic equilibrium equation is solved using a relative background dielectric constant of 45 under the short circuit boundary conditions at the top surface and the bottom interface [75]. For solving the mechanical equilibrium eqation, the mixed-typed boundary condition for epitaxial thin films is employed using elastic constants [70] of $c_{11} = 2.3 \times 10^{11}$ Pa, $c_{12} = 0.9 \times 10^{11}$ Pa and $c_{44} = 7.6 \times 10^{10}$ Pa . In the in-plane directions of the system, the two-dimensional periodical boundary condition is adopted.

We focus on $(001)_{pc}$-orientied $K_{0.5}Na_{0.5}NbO_3$ thin film in this work (“pc” stands for pseudocubic), whose Landau coefficients, elastic stifness and electrostrictive coefficients can be found in literatures [45,67]. The simulation system is discretized into $128\Delta x \times 128\Delta y \times 36\Delta z$ grid points with the grid size $\Delta x = \Delta y = \Delta z = 1$ nm for establishing the phase diagrams and investigating the superdomains. For generating the representative domain structures in Fig. 2, we adopt a larger system size

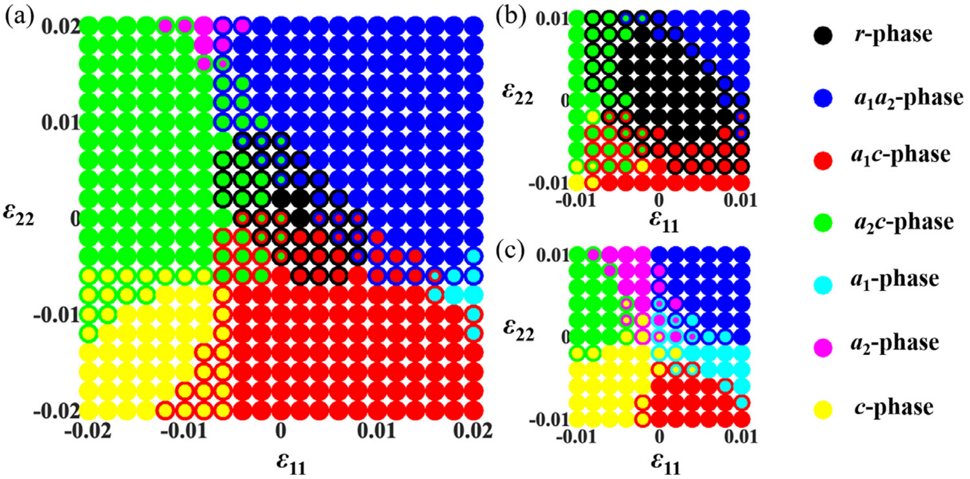

Fig. 1. The misfit strain-misfit strain phase diagrams of (001)-oriented KNN thin films established through phase-field simulations at different temperatures (a) 300 K, (b) 200 K, and (c) 600 K.

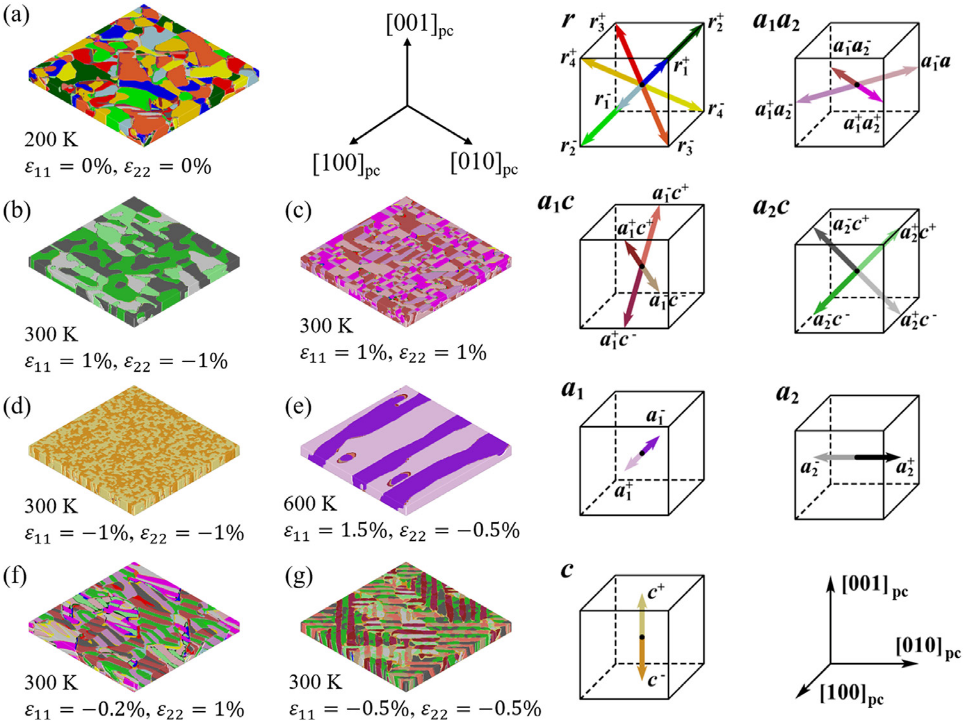

Fig. 2. Typical domain structures of (001)-oriented KNN thin films for (a) *r*-phase, (b) a_2c-phase, (c) a_1a_2-phase, (d) *c*-phase, (e) a_1-phase, (f) a_1a_2/a_2c mixed phases and (g) a_1c/a_2c mixed phases. The corresponding naming of phases is consistent with Fig. 1. The domains are colored by the direction of polar vectors as labeled on the right.

($256\Delta x \times 256\Delta y \times 36\Delta z$, $\Delta x = \Delta y = \Delta z = 1$ nm) for aesthetic purposes. In all the simulations, the thicknesses of the KNN thin film and the substrate are 20 nm and 12 nm, respectively. The equilibrium domain structure is obatined through the iteration of the TDGL equation from an initial random noise of polarization (for phase-diagram construction in Fig. 1 and all domain structures in Fig. 2) or a preset domain structure (for all superdomain strucrures in Figs. 3–7) for sufficient numbers of time steps until the total free energy is converged. In most simulations, the *x* and *y* axis corresponds to $[100]_{pc}$ and $[010]_{pc}$, respectively, except for the configurations with antiparallel superdomain polarization (Fig. 4c and row 5–10 of Table A.1) wherein the system is rotated by 45° around the *z* axis ($x//[110]_{pc}$, $y//[\bar{1}10]_{pc}$, and $z//[001]_{pc}$) to accommodate the domain patterns to the in-plane periodical boundary conditions.

3. Results

3.1. Misfit strain-misfit strain phase diagrams

To establish the phase diagrams of KNN thin films, we perform a series of phase-field simulations to obtain the equilibrium domain structures at various anisotropic misfit strains (ranging from -2.0% to 2.0%) and temperatures (T = 200K, 300K, and 600K). We classify the obtained domain structures by considering seven ferroelectric phases with distinct local polarization vectors, including the *r*-phase (P_1, P_2, P_3), a_1a_2-phases (P_1, P_2, 0), a_1c-phase (P_1, 0, P_3), a_2c-phase (0, P_2, P_3), a_1-phase (P_1, 0, 0), a_2-phase (0, P_2, 0), and *c*-phase (0, 0, P_3). Notably, due to the anisotropic biaxial misfit strains, the *r*-phase has the triclinic symmetry (space group P1), the a_1a_2-, a_1c-, and a_2c-phases have the monoclinic symme-

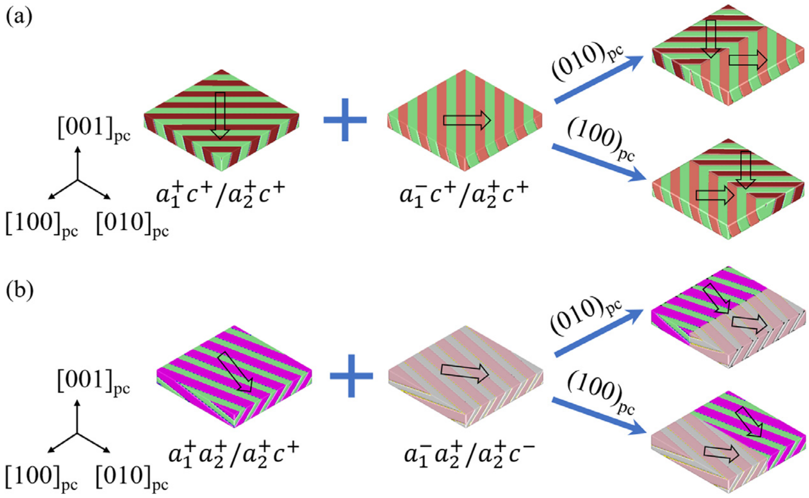

Fig. 3. Schematics for the construction of (a) the stripe-like superdomain from two single-bundle a_1c/a_2c-type polytwin structures and (b) the herringbone-like superdomain from two a_1a_2/a_2c-type polytwin structures in KNN thin films. For each case, two possible combinations are considered with the superdomain wall plane parallel to $(010)_{pc}$ or $(100)_{pc}$.

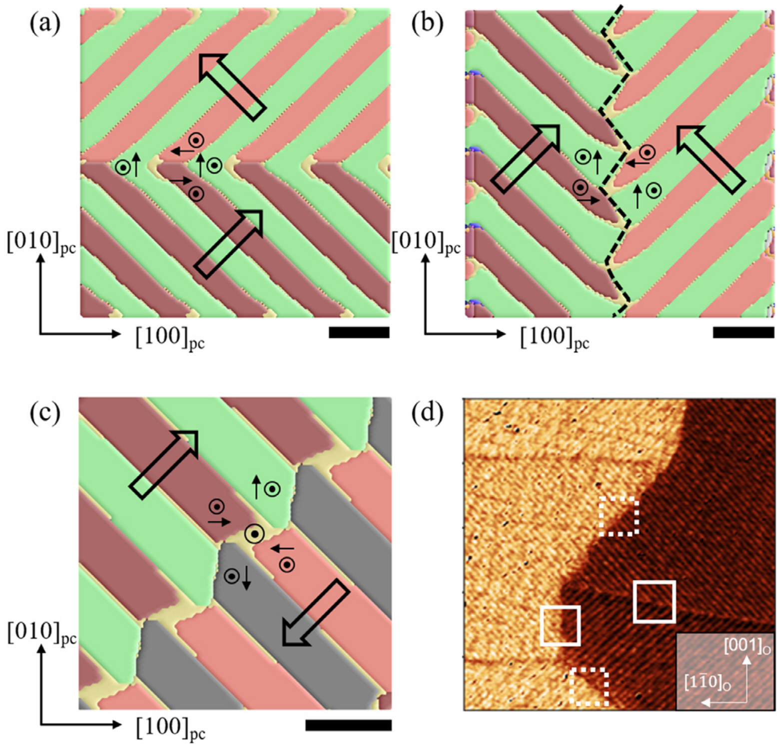

Fig. 4. Different types of the a_1c/a_2c superdomains in KNN thin films. (a–c) The simulated 90° superdomains with (a) head-to-tail (b) head-to-head configurations and (c) the antiparallel superdomain. The small arrows in each domain denote the polarization direction. The large empty arrows represent the overall polar direction of a single polytwin structure. The scale bars in (a–c) represent 25 nm. The simulated domain structures in (a–c) assume an in-plane misfit strain of $\varepsilon_{11} = \varepsilon_{22} =$ -0.5%. (d) Lateral piezoresponse force micrograph of a $K_{0.7}Na_{0.3}NbO_3$ film on $(110)_O$ $TbScO_3$ substrate. The dashed and solid squares represent the 90° and 180° superdomain walls. The image area in (d) is around 2.5 μm × 2.5 μm. Image (d) is by courtesy of Dr. Martin Schmidbauer and Dr. Jutta Schwarzkopf at IKZ Berlin.

try (Pm), and the a_1-, a_2-, and c-phases have the orthorhombic symmetry (P2mm) in general [76]. Following previous works [69], the a_1c-, and a_2c-phases are named as the M_C phase to distinguish from the a_1a_2-phase. The phase coexistence is determined by the volume fraction of the minor phase with a criterion of 20%. For example, if a simulated domain structure contains >20% of c-phase aside from the major a_1c-phase, it would be regarded as a coexisting state of the a_1c- and c-phases. Following this procedure, the misfit strain-misfit strain phase diagrams at different temperatures are constructed as shown in Fig. 1. Each point in the diagrams represents one independent simulation at the corresponding combination of misfit strains and temperature. Typical domain structures at selected temperature and misfit strain states are given in Fig. 2.

Fig. 1(a) shows the multidomain stability phase diagram of KNN thin films under anisotropic misfit strains at room temperature. We can identify seven single-phase regions labeled by uniformly colored disks and various two-phase and three-phase regions as denoted by multiple-colored disks. This multidomain phase diagram appears similar to the phase diagram calculated by thermodynamic calculations under the monodomain assumption [67] and the polydomain phase diagram computed by using the strain phase separation theory [69]. However, remarkable differences can be seen in several aspects. First, the r-phase region at the center of the diagram is much narrower than that of the monodomain phase diagram. Several phase-coexisting regions are surrounding the r-phase, which cannot be captured with the single-phase, single-domain assumption. The strain phase separation theory predicts a triangular region at the center of the polydomain phase diagram for coexisting a_1c-, a_2c-, and a_1a_2-phases [69], which is absent in the multidomain phase diagram here. Second, there are several two-phase regions between the monoclinic and orthorhombic phases (e.g., a_2c-phase and c-phase) near their boundaries, which have not been seen in the monodomain or polydomain phase diagrams [67,69]. Third, the stability range of the phase-coexisting regions between any two of the three monoclinic phases (e.g., a_1c-phase and a_2c-phase), which have also been predicted in the polydomain phase diagram [69], is much more reduced here. These differences are understandable because the phase-field simulations explicitly consider the inhomogeneous elastic strain energy and the gradient energy associated with the domain structures, which are not considered in the other two methods. The presence of these short-range interactions can modify the nature of phase transitions, leading to the coexistence of several polymorphic ferroelectric phases. Similar behaviors have been known in phase-field simulations of $BaTiO_3$ [77] and $PbTiO_3$ thin films [78]. In fact, nanodomains of multiple polymorphic phases in epitaxial ferroelectric thin films have been observed in experiments [79–81]. In this sense, the multidomain stability phase diagram based on phase-field simulations can present a more accurate physical description of the system of interest than the analytical approaches.

The stability of the ferroelectric phase changes with temperature, as seen in the phase diagram at lower (200 K) or higher (600 K) temperatures in Fig. 1(b and c). At the low temperature, the r-phase region expands along with the surrounding multi-phase regions, suggesting enhanced stability of the r-phase upon decreasing the temperature consistent with the phase transition order in bulk KNN [82]. At the high temperature, the r-phase region shrinks and completely disappears at 600 K. The central region of the diagram becomes a junction of the other single-phase regions, including three orthorhombic phases, i.e., a_1-, a_2- and c-phases, and three monoclinic phases, i.e., a_1c, a_2c, and a_1a_2, which results in new types of phase coexistence. Note that the misfit strain-misfit strain diagram of KNN thin films at 600 K resembles that of tetragonal $BaTiO_3$ at room temperature [77] due to the intrinsic structural similarities of the two materials in their bulk states [82]. In an earlier work, we have established the temperature-misfit strain phase diagrams of KNN thin films subject to equal-biaxial misfit strains using the phase-field method [45]. The results here complement the previous one for anisotropic misfit strain states, yielding more comparable results with the KNN films grown on the $(110)_O$-oriented scandate substrates in experiments. Note that the present results along the diagonal of the diagrams are generally consistent with Ref. [45].

3.2. Typical domain structures

Typical domain structures obtained by the phase-field simulations at selected temperatures and misfit strains are given in Fig. 2, corresponding to the single-phase and two-phase regions in the phase diagrams. As these domain structures are obtained by quenching the system from a random noise of polarization, all the energy-favorable domain variants have an equal propensity to develop and exhibit approximately equal volume fractions at equilibrium. For example, the r-phase (Fig. 2(a)) includes eight degenerate domain variants ($r_1^{\pm} - r_4^{\pm}$). The domain pattern is mosaic, and the domain walls may be distorted from the permissible planes due to the nonuniform elastic strains. This irregular domain structure is similar to that of rhombohedral $BiFeO_3$ epitaxial films grown on $(001)_{pc}$-oriented $SrTiO_3$ substrates with no miscut angle [14]. Fig. 2(b) shows a domain structure of the a_2c-phase, which contains four degenerate domain variants ($a_2^+c^+, a_2^+c^-, a_2^-c^+, a_2^-c^-$). The ferroelastic domain walls separating the domain variants with reversed out-of-plane polarization components (e.g., between $a_2^+c^+$and $a_2^+c^-$) are meandering, whereas the domain walls associated with the reversal of in-plane polarization components (between $a_2^-c^+$and $a_2^+c^+$) are generally straight along $[010]_{pc}$. The a_1a_2-phase (Fig. 2(c)) displays a typical domain structure consisting of four a_1a_2 variants of pure in-plane polarization separated by ferroelastic domain walls parallel to $[100]_{pc}$ or $[010]_{pc}$ and non-ferroelastic domain walls parallel to $[\pm1\pm10]_{pc}$. The domains of the orthorhombic phases, e.g., a_1-phase and c-phase, only exhibit ferroelectric domains with antiparallel polarization, as shown in Fig. 2(d and e). The domain walls are meandering in the c-phase while are generally straight along the stretching direction in the a_1-phase. The domain structures of the other two single-phase regions shown in Fig. 1, i.e., the a_2- and a_1c-phases, are omitted in Fig. 2 since they are equivalent to the domain structures of a_1- and a_2c-phases, respectively, by a mirror symmetry operation to the diagonal of the diagram. Notably, some of these single-phase domain structures require large tensile (e.g., a_1a_2-phase) or highly anisotropic biaxial misfit strains (e.g., a_2c- and a_1-phases) to be stabilized at room temperature, which is challenging to realize in experiments. Nevertheless, the formation of c-phase has been reported in KNN films epitaxially grown on $SrTiO_3$ [66] and $DyScO_3$ [41] substrates that can impose large biaxial compressive strains to the films, which agrees well with the predicted stability range in Fig. 1(a) and thus supports our theoretical results.

Domain structures with more complex patterns may form in the two-phase regions, as shown in Fig. 2(f and g) for the a_1a_2/M_C and a_1c/a_2c phases, respectively. The domains in the a_1c/a_2c phase stabilized by moderate biaxial compressive misfit strains consist of several patched regions with stripe-like domain patterns. At the boundary between two sets of stripes, the stripe patterns may be perpendicular to and extend continuously across the boundary or be inclined to the boundary by 45°. The domain structures in the a_1a_2/M_C phase region stabilized by biaxial anisotropic misfit strains also contain patched areas with stripe-like patterns. However, these stripes extend along a high-index direction between $[0\pm10]_{pc}$ and $[\pm1\pm10]_{pc}$, thus forming the herringbone-like patterns when the two bands meet at $\{100\}_{pc}$ planes.

3.3. Construction of superdomains by two sets of polytwin structures

These two complex domain structures (Fig. 2(f and g)) resemble the stripe-like and herringbone-like superdomains observed in KNN epitaxial thin films by piezoresponse force microscopy (PFM) despite of differences in the chemical compositions, misfit strains, and film thicknesses [43,58]. However, apparent differences manifest in two aspects. First, no significant contrast in the phase images of vertical PFM for both the herringbone-like and stripe-like superdomains are observed in experiments [43,58], suggesting that the out-of-plane polarization direction should be uniform across the sample. In contrast, the simulation results contain all degenerate domain variants with antiparallel reversed vertical polarization. Second, the domain patterns in experiments are regular and extend to more than one micron, forming hierarchical superdomain structures with well-defined boundaries. In contrast, the simulated domain bundles are confined within tens of nanometers in lateral size and are randomly distributed. These discrepancies may be due to the finite size of the simulation box (256 nm) and the fact that the kinetic factors may favor the nucleation and formation of certain domains during the film growth, which is not considered in the simulations from a random noise initial state.

To better capture the structural features of the superdomains in simulations, we manually construct a polytwin structure consisting of a pair of ferroelastic domains as the initial state and relax the system to obtain the equilibrium structure. Possible polytwin structures of the a_1c/a_2c and $a_1a_2/\mathrm{M_C}$ phases have been obtained in this way elsewhere [69]. Then, we explore possible combinations of two polytwin structures to create the superdomain structure. Two examples are shown in Fig. 3 for the stripe-like and herringbone-like superdomains. Take the combination of $a_1^+c^+/a_2^+c^+$ and $a_1^-c^+/a_2^+c^+$ polytwins as an example. The in-plane components of the overall polarization of $a_1^+c^+/a_2^+c^+$and $a_1^-c^+/a_2^+c^+$ polytwins are along $[110]_{\mathrm{pc}}$ and $[\bar{1}10]_{\mathrm{pc}}$, respectively, as labeled by the empty black arrows in Fig. 3(a). The polytwin bundles can be regarded as two "single-domains" with uniform polarization vectors, which can be weld together along either $(010)_{\mathrm{pc}}$ or $(100)_{\mathrm{pc}}$ plane to form the head-to-head or head-to-tail configurations, respectively. For convenience, we call these two types of superdomains charged and uncharged 90° superdomains, respectively. If the overall in-plane polarization of the two polytwin structures are antiparallel, such as that for $a_1^+c^+/a_2^+c^+$and$a_1^-c^+/a_2^-c^+$ polytwins, the superdomain structures can be constructed by welding the two bundles along $(110)_{\mathrm{pc}}$ or $(1\bar{1}0)_{\mathrm{pc}}$ planes, forming the 180° superdomains with either head-to-head or antiparallel configuration (Table A.1). Likewise, we follow a similar procedure for the $a_1a_2/\mathrm{M_C}$ superdomains to obtain the head-to-tail and head-to-head configurations, as shown in Fig. 3b. We have enumerated all possible combinations of two polytwin structures of the a_1c/a_2c and a_1a_2/a_2c phases and list the unrepeated cases in Tables A.1 and A.2 for the stripe-like and herringbone-like superdomains, respectively. It should be noted that the naming of superdomain walls by the angle of the overall polarization of the neighboring polytwins, e.g., "90°" and "180°", are used in a sense only for the two-dimensional in-plane view. In general, the overall polarization of the polytwin bundles also have net out-of-plane components and thereby are not rigorously 90° or 180° rotated from each other in three-dimension. Nevertheless, we will adopt this naming hereafter for convenience.

3.3.1. The stripe-like a_1c/a_2c superdomains

We first focus on the a_1c/a_2c superdomains. As mentioned above, the out-of-plane polarization in the a_1c/a_2c superdomains is uniform in experiments. Therefore, without losing generality, we consider the case where the out-of-plane polarization is all upward. According to Table A.1, only four superdomain structures (row 1-2 and row 5-6) possess overall upward out-of-polarization, three of which with the least total energy densities are presented as the planar view in Fig. 4(a–c). We discussed the relaxation of these three preset domain structures in Fig. A1 of Appendix and compared them with the quenching case starting from random noises, the result of which suggests the formation of regular domain structures is energetically favorable.

The two 90° superdomains (Fig. 4(a and b)) have the boundaries parallel to $[100]_{\mathrm{pc}}$ or $[010]_{\mathrm{pc},}$ while the antiparallel case (Fig. 4(c)) has the boundary along the diagonal direction, i.e., $[\pm1\pm10]_{\mathrm{pc}}$. These orientations of superdomain boundaries have also been observed in experiments. For example, the lateral piezoresponse force microscopy (LPFM) phase image of 35 nm-thick $\mathrm{K_{0.7}Na_{0.3}NbO_3}$ grown on $\mathrm{TbScO_3}$ substrates also shows two types of interfaces between two the neighboring stripe-like polytwins, which are along the horizontal/vertical (labeled by solid white boxes) or diagonal directions (labeled by dashed white boxes), as shown in Fig. 4(d). Therefore, one can distinguish the 90° superdomain walls and the 180° superdomain walls by the overall orientation of these boundaries. However, for 90° superdomain walls, it is still challenging to determine whether the horizontal/vertical boundaries seen in experiments are charged (head-to-head or tail-to-tail) or uncharged (head-to-tail) superdomain walls.

The simulation results can provide some insights to identify the two cases. First, the head-to-tail superdomain structure has lower total energy than the head-to-head counterpart (Table A.1), suggesting higher stability of the uncharged superdomain walls from the energy perspective. Second, the two types of 90° superdomain walls have distinct morphological features locally. As shown in Fig. 4, the superdomain wall is flat for the head-to-tail case but is rugged for the head-to-head counterpart. In the latter, the formation of the zigzag boundary (dashed segments in Fig. 4(b)) and domains with sharp ends at the junctions (domains in marron and salmon colors) helps to maintain the head-to-tail configuration of local polarization vectors near the superdomain wall for lowering the electrostatic energy. Therefore, although the head-to-head superdomain wall seems to be charged macroscopically (as seen from the large empty vectors), it consists of segmented domain walls principally charge-neutral (this, however, does not mean they have zero bound charge density). Therefore, one can distinguish the charged and uncharged 90° superdomain walls by examining their microscopic morphological features, provided that the experimental technique has a sufficiently high spatial resolution (e.g., $\leq$ 10 nm). Notably, the boundary of the antiparallel superdomains (Fig. 4(c)) is also rugged. We can see a quadrant domain structure with a pair of threefold vertices instead of a fourfold vertex at the junction of the four monoclinic domain variants. This behavior is consistent with the three-state Potts model proposed by Srolovitz and Scott for quadrant closure domains [83,84].

It is also interesting to examine the polarization distributions within the superdomain wall planes. We plot the polarization configurations in the cross-section planes at the center of the superdomain walls in Fig. 5 (a–c), corresponding to the three cases in Fig. 4(a–c). For each case, the schematics of the side view of the two neighboring polytwins are presented (Fig. 5(d–f)). For all cases, we find that there are domains and domain walls within the superdomain wall planes, as shown by the modulated reddish and blueish regions in Fig. 5(a–c). For the superdomain wall of the head-to-head case (Fig. 5b), the domains within the superdomain wall plane match with the two neighboring polytwins, i.e., the domain walls are inclined to $[001]_{\mathrm{pc}}$ by the same angle φ. However, the adjacent polytwins are incoherent for the other two cases (Fig. 5(d–f)), resulting in distinct polarization configuration in the superdomain wall plane (Fig. 5(a–c)). For example, the domain walls are inclined to the $[001]_{\mathrm{pc}}$ directions by $+\varphi$ and $-\varphi$ in the two adjacent polytwins in Fig. 5(d) while the walls in Fig. 5(a) are vertical near the film surface and bifurcates at the bottom (denoted by dashed segments). Similarly, the incoherent polytwin patterns at the junction result in modulated polarization distribution in the superdomain walls (Fig. 5(c)). These findings reveal that there are nontrivial local polarization configurations within the superdomain wall plane, which embodies the idea of "domains in domains and walls in walls" [85].

3.3.2. The herringbone-like $a_1a_2/\mathrm{M_C}$ superdomains

We then turn to the $a_1a_2/\mathrm{M_C}$ superdomains that exhibit the herringbone-like pattern. Note that similar patterns with nested domains of non-45° inclination to the superdomain boundary have also been termed as chevron-like structures in other ferroelectric materials [30,32]. Without losing generality, we focus on the a_1a_2/a_2c superdomains. Among all the cases in Table A.2, we present cases where the herringbone-like pattern can be identified in Fig. 6(a–c). The relaxation process of these representative a_1a_2/a_2c superdomain structures from the preset patterns is presented in Appendix (Fig. A2). The superdomain structures in Fig. 6(a) and (b) are equivalent by swapping the $a_2^+c^+$ and

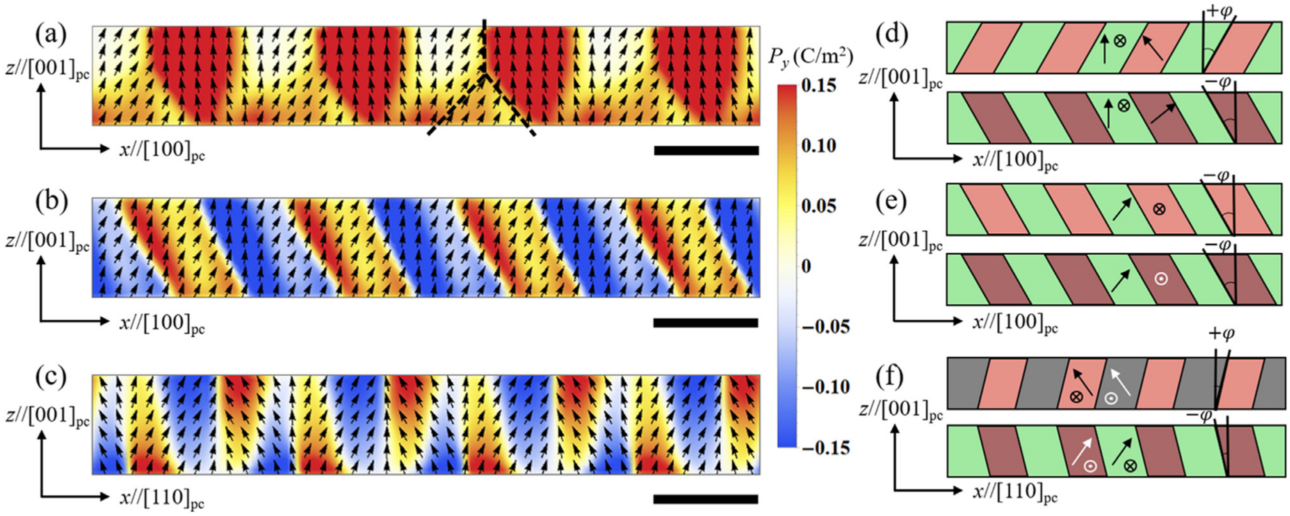

Fig. 5. Cross section views of the simulated a_1c/a_2c superdomains in KNN thin films. (a–c) Polarization distribution in the superdomain wall plane of the superdomain structures corresponding to Fig. 4(a–c). (d–f) Schematics of the domain structures of the two polytwin structures adjacent to the superdomain walls in (a–c). The arrows in each domain denote the polarization direction. The scale bars in (a–b) represent 20 nm.

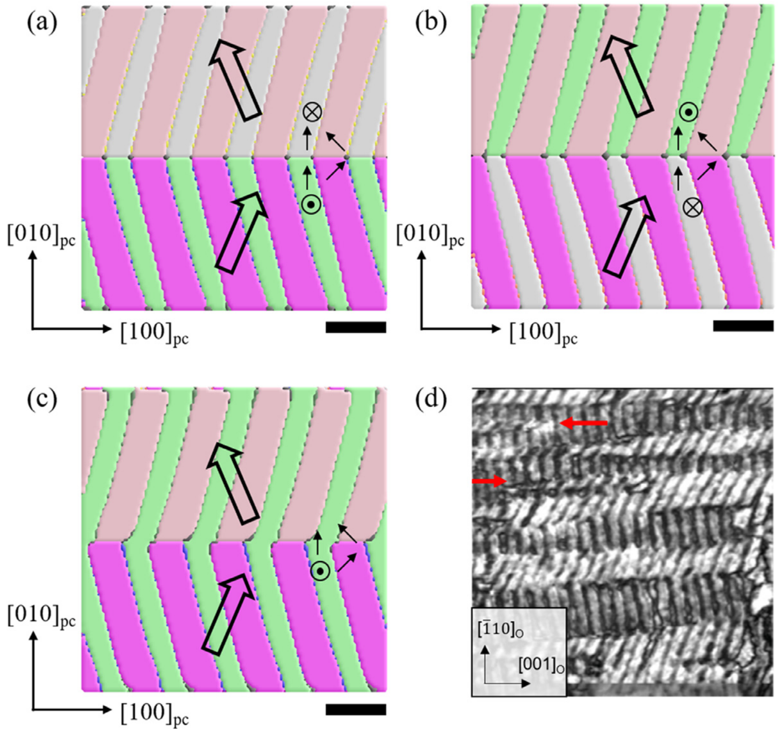

Fig. 6. Different types of a_1a_2/a_2c superdomains in KNN thin films. (a–c) The simulated superdomains consisting of (a) $a_1^+a_2^+/a_2^+c^+/a_1^-a_2^+/a_2^+c^-$, (b) $a_1^+a_2^+/a_2^+c^-/a_1^-a_2^+/a_2^+c^+$, and (c) $a_1^+a_2^+/a_2^+c^+/a_1^-a_2^+/a_2^+c^+$ domains. (a,b) have zero net out-of-plane polarization while (c) has positive overall out-of-plane polarization. The small arrows in each domain denote the polarization direction. The large empty arrows represent the overall polar direction of a single polytwin structures. The scale bars in (a–c) represent 25 nm. The simulated domain structures in (a–c) assume an in-plane misfit strain of ε_{11} = -0.2% and ε_{22}= 1.0 %. (d) Lateral piezoresponse force micrograph of a $K_{0.9}Na_{0.1}NbO_3$ film on $(110)_O$ $NdScO_3$ substrate. The red arrows denote the termination of a polytwin bundle. The image area in (d) is around 1.0 μm × 1.0 μm. Image (d) is by courtesy of Dr. Martin Schmidbauer and Dr. Jutta Schwarzkopf at IKZ Berlin. (For interpretation of the references to color in this figure legend, the reader is referred to the web version of this article.)

$a_2^+c^-$ domains and hence have the identical total energy. They are shown as an example to demonstrate possible degenerate states which exhibit the same morphology. The superdomains in Fig. 6(c) can be regarded as a “poled” state of either Fig. 6(a) either ... or ... (b) by a large electric field along $[001]_{pc}$ that can switch the $a_2^+c^-$domains to the $a_2^+c^+$domains. Another equivalent downwardly polarized state with only $a_2^+c^-$domains is omitted. Other symmetrically equivalent combinations of the a_1a_2/M_C polytwins can be classified either into the “unpoled” (e.g., Fig. 6(a and b)) or the “poled” cases (Fig. 6(c)). The rest combinations with head-to-head configurations, as shown in Table A.2, generally have much larger energy densities than the cases shown here and will not be discussed hereafter.

In all three cases, the global polarization vectors of the adjacent polytwin bundles (denoted by large empty arrows) are in head-to-tail configuration across the horizontal superdomain walls. Therefore, the overall domain structures are also polarized along $[010]_{pc}$. Notably, for all cases in Fig. 6, the superdomain walls are

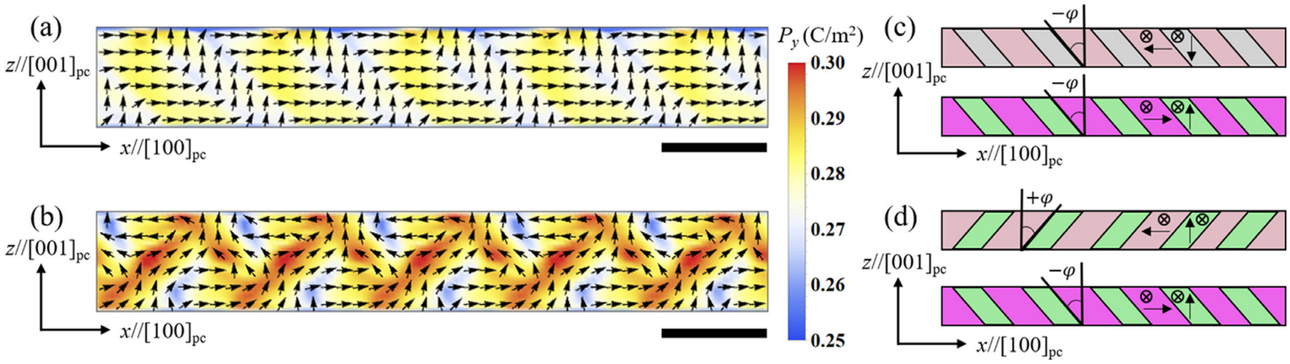

Fig. 7. Cross section views of the simulated a_1a_2/a_2c superdomains in KNN thin films. (a and b) Polarization distribution in the superdomain wall plane of the superdomain structures corresponding to Fig. 6(a)and (c). (c and d) Schematics of the domain structures of the two polytwin structures adjacent to the superdomain walls in (a and b). The arrows in each domain denote the polarization direction. The scale bars in (a–b) represent 20 nm.

flat and sharp, in contrast to the rugged boundaries in Fig. 4(b and c). A quantitative evaluation of the superdomain wall width will be given in the Discussion. The local polarization vectors near the superdomain wall also exhibit head-to-tail configurations near the superdomain walls. In experiments, the herringbone-like pattern consisting of a set of $a_1a_2/\mathrm{M_C}$ polytwin bundles have been revealed in 30 nm-thick $K_{0.9}Na_{0.1}NbO_3$ thin films grown on $NdScO_3$ substrates (Fig. 6(d)). We highlight two morphological features. There are alternating bright and dark stripes within each polytwin bundle, which corresponds to the a_1a_2 and $\mathrm{M_C}$ type domain variants, respectively. The $\mathrm{M_C}$ domains are much thinner than the a_1a_2 domains in experiments, while they are similar in the simulations. This discrepancy is understandable because this ratio of the domain width is a function of the anisotropic misfit strains, as shown in Ref. [69], which may differ in the present simulations from the experiments. Moreover, due to the ultrathin nature of the $\mathrm{M_C}$ domains in experiments, it is challenging to distinguish whether the observed herringbone pattern in Fig. 6(d) is the poled or unpoled states. Considering the small differences in the total free energy densities of the three states (Table A.2), it is entirely possible that the observed herringbone structure is a mixture of the poled and unpoled states, thereby containing four combinations in general (Fig. 6(a–c) and the omitted downwardly poled case). Notably, there are discontinuities in the herringbone pattern in experiments, as indicated by red arrows in the LPFM images in Fig. 6d, which may be related to the multiple combinations of the $a_1a_2/\mathrm{M_C}$ polytwin bundles.

The cross-section view of the superdomain walls and the corresponding polarization distribution within the plane for the herringbone-like structures are presented in Fig. 7. We find that the polarization configuration at the sharp superdomain wall of the unpoled case in Fig. 7(a) is identical with the neighboring polytwins due to the coherent domain wall orientations at the junctions (Fig. 7(c)), i.e., they are both tilted with respect to $[100]_{pc}$ by $-\varphi$. In contrast, the polarization distribution within the "poled" superdomain wall plane exhibits complex topological features (Fig. 7(b)). This is because the domain walls of the neighboring polytwins are incoherent, i.e., they are tilted with respect to $[100]_{pc}$ by $+\varphi$ and $-\varphi$ respectively.

The two types of superdomain structures presented above demonstrate that the superdomain walls can be flat and have a well-defined orientation globally and simultaneously possess subtle features at the local length scale. These multiscale features are reminiscent of the rough nature of conventional domain walls, which can be straight globally but with kinks locally [86,87]. Unlike the conventional domain walls, however, the superdomain wall plane may host modulated polarization distributions with nontrivial topological features. The presence of nanodomains and domain walls within a superdomain wall may be associated with intriguing properties and deserve further theoretical and experimental explorations.

4. Discussion

In the following, we draw a further analogy between the superdomain walls and the normal domain walls by discussing the width of superdomains and the bound charge distributions across the walls.

4.1. Width of the superdomain walls

We first evaluate the width of the superdomain wall. For a conventional domain wall of a ferroelectric, the domain wall width can be obtained from the polarization profile across the wall [88,89]. Similarly, for the superdomain wall, we can plot the overall polarization profile averaged within each plane parallel to the superdomain wall plane. For example, for the a_1c/a_2c superdomain with the head-to-tail configuration in Fig. 4(a), the polarization is averaged within the $(010)_{pc}$ plane to obtain the one-dimensional profile across the superdomain wall as plotted in blue dots in Fig. 8(a). Similar profiles can be obtained for the other superdomains in Figs. 4 and 6. For each case, the width of the superdomain wall is determined by the tangent construction used for determining the thickness of a diffuse interface [88,90], as labeled in Fig. 8. It is seen that the three $a_1a_2/\mathrm{M_C}$ superdomain walls are relatively sharp (~ 1.8 – 3 nm) comparable with a conventional ferroelectric domain wall (~ 1 – 3 nm). In contrast, the walls of the a_1c/a_2c superdomains are much wider, e.g., 7.0 nm and 8.6 nm for the head-to-tail and antiparallel superdomains, respectively. Nevertheless, the 180° superdomain walls are thicker than the 90° counterpart, which is also typical for conventional domain walls of ferroelectric materials such as $PbTiO_3$ [91] and $BaTiO_3$ [92]. The head-to-head superdomain wall has a remarkably wide thickness (> 40 nm) and reduces the magnitude for the overall polarization in the neighboring polytwins. Note that for conventional domain walls, the charged walls are also much thicker than the neutral ones [93,94].

We also note that the superdomain wall profile is symmetric to the center of the polytwin except for the head-to-head superdomain wall of the a_1c/a_2c superdomains. This asymmetry suggests that the tail-to-tail superdomain wall, which forms at the two ends of the simulated system due to the periodic boundary condition, is intrinsically inequivalent to the head-to-head counterpart. A detailed comparison between the head-to-head and tail-to-tail superdomains is beyond the scope of the present study.

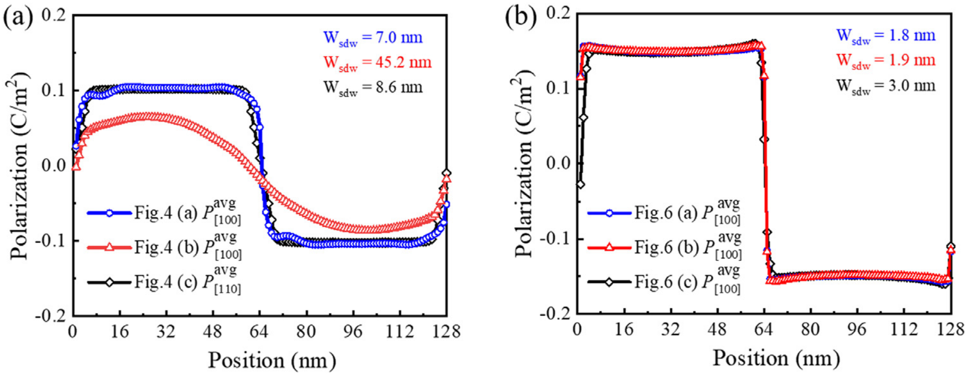

Fig. 8. Profiles of the averaged polarization across the superdomain walls of (a) the a_1c/a_2c and (b) a_1a_2/a_2c superdomains. The profiles are drawn along the direction perpendicular to the superdomain wall plane.

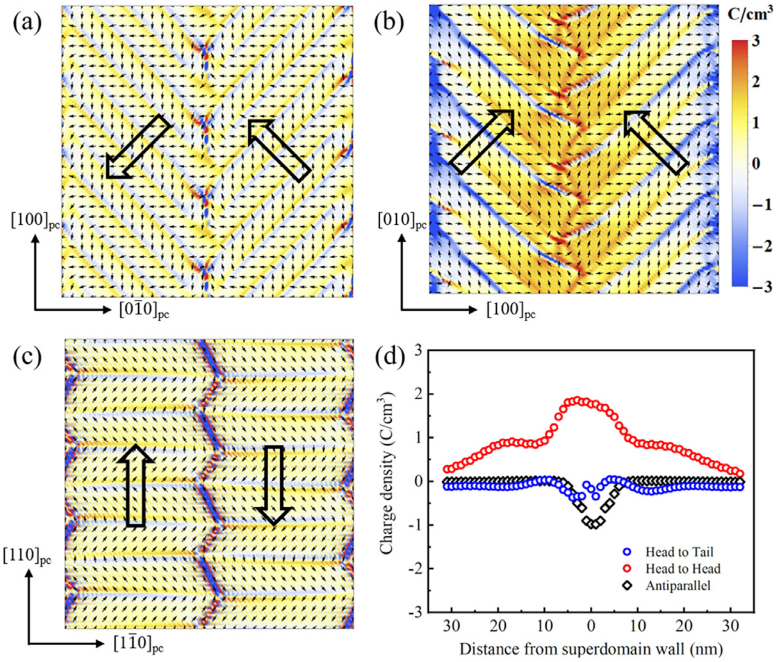

Fig. 9. Bound charge density mapping at the superdomain walls. (a–c) The calculated bound charge density ρ_b distributions in the center layer of KNN thin films for the stripe-like superdomains corresponding to in Fig. 4(a–c), respectively. (d) The profiles of averaged ρ_b across the superdomain walls.

4.2. Bound charges at the superdomain walls

The conventional domain walls in ferroelectric materials are movable interfaces that can exhibit larger susceptibility than the surrounding domains [95], host free carriers and become electrical conductive [94], and enhance photovoltaic effects [92], thus holding promises for novel nanoelectronics applications. Here, we propose that the superdomain wall can also be conductive or insulating, depending on the configurations.

The domain wall conduction is ascribed to the uncompensated bound charges near the wall (measured by the volumetric density $\rho_b = -\nabla \cdot \boldsymbol{P}$), which results in free carriers accumulating and thus rendering the wall to be conductive. Therefore, we evaluate the distributions of the bound charge density ρ_b for all the superdomains shown in Figs. 4 and 6. Since the spontaneous polarization tends to relax near the surface and interface regions and yield bound charge density not intrinsic to the domain walls, we only examine the mapping of ρ_b in the center layer of the film to have a relatively conservative estimation of ρ_b. The results for the three a_1c/a_2c superdomains are shown in Fig. 9 while the corresponding one-dimensional profiles across the superdomain walls are also presented. We can see that the head-to-tail superdomain wall generally has negligible bound charge, except for some local hot spots at the domain vertices. In contrast, the head-to-head superdomain wall is associated with considerable positive bound charge density that extends to ~30 nm away from the superdomain wall plane. Therefore, this type of superdomain wall may be much more conductive to electrons than the uncharged counterpart, which can be utilized to distinguish these two types of 90° superdomain walls in experiments, e.g., by using the conductive atomic force microscopy [96]. For the 180° antiparallel case, we find that even though the superdomain is globally uncharged, it is locally charged with alternating positive and negative ρ_b along the zigzag boundary. This configuration may lead to spontaneous separation of electrons and holes and can be regarded as an array of nanoscale p-n junctions that may be useful for diode applications [97]. The ρ_b for the three $a_1a_2/\mathrm{M_C}$ superdomains are generally not appreciable as the a_1c/a_2c cases, which may be ascribed to their smaller thicknesses, and thus are not shown. These findings suggest that the superdomain walls may bring new insights to creating conductive channels in the domain wall-based nanoelectronics [33]. It would be interesting to verify the predicted superdomain wall conduction in KNN and other materials and further explore the creation and dynamical control of the superdomain walls.

4.3. The analogy between domain walls and superdomain walls

Based on our findings, we would like to summarize a few similarities and differences between the conventional domain walls and the superdomain walls in ferroelectric thin films. Both interfaces usually have well-defined orientations macroscopically but also exhibit subtle morphological features at a finer scale. Like the conventional domain walls, the superdomain wall can also be described by a hyperbolic tangent-like profile and shows different energies and widths depending on the rotation angle of the overall polarization across the wall. The superdomain wall can be as sharp as a conventional domain wall (1–3 nm) or much wider (6 – 9 nm) even in the uncharged configuration. There might be intriguing textures of ferroelectric polarization within the superdomain wall plane absent in conventional domain walls. The charged superdomain wall can be even wider and may give rise to considerable electrical conductivity. Besides, even though the presently studied superdomain walls are Ising-like, it is entirely possible to expect the discovery of chiral superdomain walls under appropriate circumstances. It is also worth to note that the orientation of a permissible domain wall for a ferroelastic can be theoretically predicted by using the mechanical compatibility condition [98,99]. Generalization to non-permissible domain walls can be realized by using the microelasticity theory [16,100]. Likewise, it would be of interests to explore the possibility for predicting the macroscopic orientation of a “permissible” or “non-permissible” superdomain boundary, such as by utilizing the nonlinear elasticity theory of structural transformation [101,102].

5. Summary

We establish the multidomain stability phase diagrams of epitaxial KNN thin films subject to anisotropic misfit strains at different temperatures by using phase-field simulations. Based on the diagrams, we identified the formation conditions and structural features of two types of superdomains with stripe-like or herringbone-like morphology, which agree very well with experiments. We demonstrate how the superdomain structures can be constructed from two sets of polytwins and thus the formation of superdomain walls. The superdomain walls not only display features analogous to the conventional domain walls, such as different energies, thicknesses, and potentially conductivity, but also exhibit unique features such as modulated polarization configurations within the superdomain wall plane. The understanding attained in the present study on the domain structures in low-symmetry ferroelectric phases can be extended to other ferroelastic/ferroelectric systems, such as the ‘chevron’ domains in $LaAlO_3$ [103] and the ‘quantum domain solid’ state in $SrTiO_3$ [104]. Moreover, the roughness at the superdomain junctions implies a fractal nature of these boundaries, which may lead to unique dynamical behaviors during domain switching [105]. Future work is anticipated on exploring the relaxational and dynamical behaviors of the superdomains and walls.

Declaration of Competing Interest

The authors declare that they have no known competing financial interests or personal relationships that could have appeared to influence the work reported in this paper.

Acknowledgment

This work was supported by “the Fundamental Research Funds for the Central Universities (WUT: 2021IVA002)”. B.W. and L.-Q.C. acknowledge support by the National Science Foundation (NSF) through Grant No. DMR-1744213. A.L. acknowledges funding from the Materials Research Science and Engineering Center (MRSEC) of The Pennsylvania State University, supported by the NSF under Grant. No. DMR-1420620. L.B. acknowledges the support by the European Community (European Regional Development Fund – ERDF) under Grant No. 1.8/15 for funding". The computer simulations were performed using the commercial software package μ-PRO (http://mupro.co) on the ICS-ACI Computing Systems at The Pennsylvania State University and at the Extreme Science and Engineering Discovery Environment cluster, which used the Comet system at the UC San Diego. The authors are grateful to Dr. Martin Schmidbauer, and Dr. Jutta Schwarzkopf at IKZ Berlin for fruitful discussions and providing the piezoresponse force microscopy images.

Appendix

Figs. A1 and A2 present the relaxation process of the three states in Fig. 3 for the stripe-like superdomains and the three states in Fig. 6 for the herringbone-like superdomains from the manually preset patterns to the equilibrium. For comparison, we also show the relaxation for the simulations under the same boundary conditions but starting from a random noise state. It is seen that, for all preset cases, the total energy quickly reduces as the simulation runs while the relaxation is much slower for the quenching cases. The energy relaxation is accompanied by the development of polarization magnitude to the equilibrium value and the adjustment of the domain wall plane orientation. Comparing to the quenching simulations, the resultant domain structures from preset domain patterns have much lower energies in general, suggesting the formation of domain structures with regular patterns is energetically favorable.

Table A.1
Possible combinations of polytwin domains for the a_1c/a_2c superdomain.

Polydomain 1	Polydomain 2	Relaxed superdomain structures	Disrupted?	Charged?	Difference in total energy density (a.u.)*
 $a_1^+c^+/a_2^+c^+$ 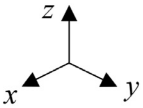	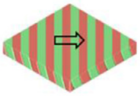 $a_1^-c^+/a_2^+c^+$ $(a_1^+c^+/a_2^-c^+)$	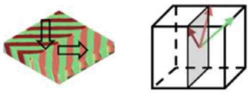	Yes	No	0
		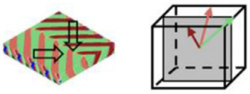	No	Yes	876
	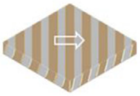 $a_1^-c^-/a_2^+c^-$ $(a_1^+c^-/a_2^-c^-)$	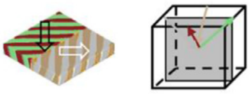	No	No	1869
			Yes	Yes	2065
	 $a_1^-c^+/a_2^-c^+$	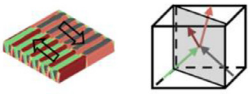	Yes	No	73
		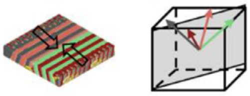	Yes	Yes	1476
	 $a_1^-c^-/a_2^-c^-$	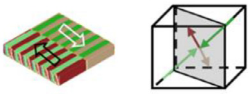	No	No	2136
		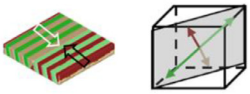	No	Yes	2202
	 $a_1^+c^-/a_2^+c^-$	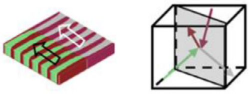	Yes	No	659
		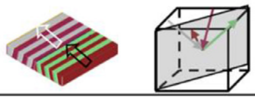	Yes	Yes	1199

---

* The total energy density for each case is relative to the minimal case.

**The domain structures in row 5 – 10 are rotated around the z-axis by 45° so that $x//[110]_{pc}$, $y//[\bar{1}10]_{pc}$, and $z//[001]_{pc}$ while in the other cases, $x//[100]_{pc}$, $y//[010]_{pc}$, and $z//[001]_{pc}$.

Table A.2.
Possible combinations of polytwin domains for the a_1a_2/a_2c superdomain.

Polydomain 1	Polydomain 2	Relaxed superdomain structures	Disrupted?	Charged?	Difference in total energy density (a.u.)*
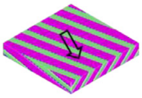 $a_1^+a_2^+/a_2^+c^+$ 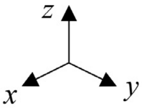	 $a_1^-a_2^+/a_2^+c^-$	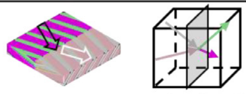	No	No	0
	 $a_1^+a_2^-/a_2^-c^+$	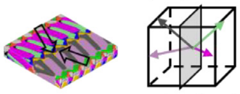	No	Yes	4621
	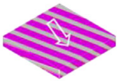 $a_1^+a_2^+/a_2^+c^-$	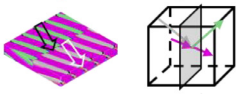	Yes	No	994
	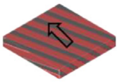 $a_1^-a_2^-/a_2^-c^+$	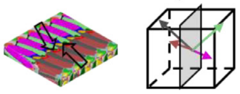	Yes	Yes	5743
	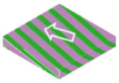 $a_1^+a_2^-/a_2^-c^-$	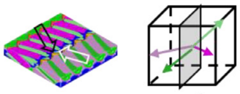	Yes	Yes	3844
	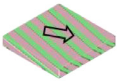 $a_1^-a_2^+/a_2^+c^+$	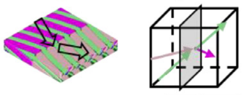	Yes	No	35
	 $a_1^-a_2^+/a_2^+c^+$	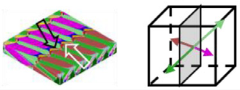	No	Yes	4804

* The total energy density for each case is relative to the minimal case.
** In all cases here, $x//[100]_{pc}$, $y//[010]_{pc}$, and $z//[001]_{pc}$.

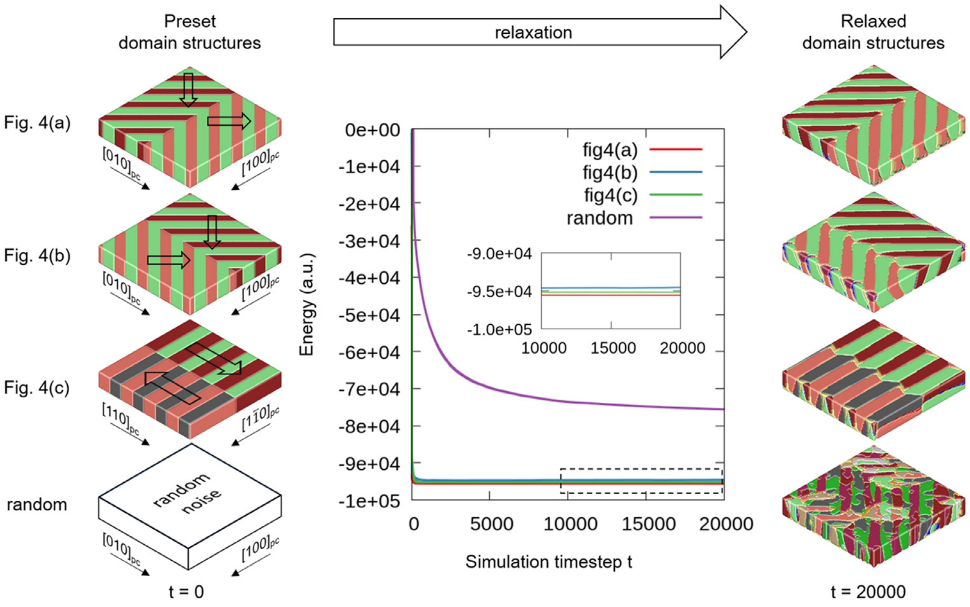

Fig. A1. Relaxation of different preset domain structures for the a_1c/a_2c superdomains in KNN thin films. The left panel shows the initial domain structures with preset polarization magnitude $|\boldsymbol{P}|$=0.2 C/m^2. The middle panel shows the variation of the total free energy with respect to the simulation timestep t. The inset shows an expanded plot for the region denoted by the dashed square. The right panel shows the final domain structures at t = 20,000.

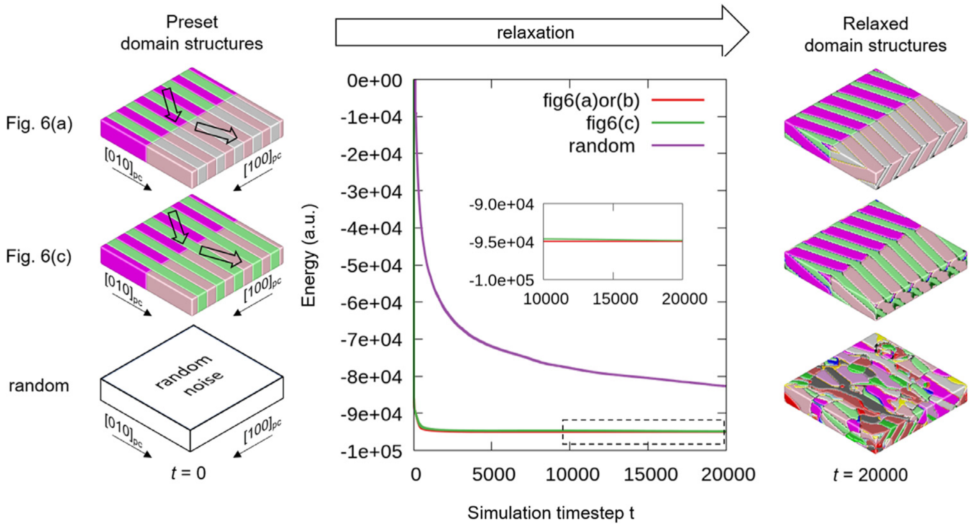

Fig. A2. Relaxation of different preset domain structures for the a_1a_2/a_2c superdomains in KNN thin films. The left panel shows the initial domain structures with preset polarization magnitude $|\boldsymbol{P}|$=0.2 C/m^2. The middle panel shows the variation of the total free energy with respect to the simulation timestep t. The inset shows an expanded plot for the region denoted by the dashed square. The right panel shows the final domain structures at t = 20,000.

References

[1] A.K. Tagantsev, L.E. Cross, J. Fousek, Domains in Ferroic Crystals and Thin Films, Springer New York, New York, NY, 2010, doi:10.1007/978-1-4419-1417-0.

[2] S. Wada, K. Yako, H. Kakemoto, T. Tsurumi, T. Kiguchi, Enhanced piezoelectric properties of barium titanate single crystals with different engineered-domain sizes, J. Appl. Phys. 98 (2005) 014109, doi:10.1063/1.1957130.

[3] M.J. Highland, T.T. Fister, M.I. Richard, D.D. Fong, P.H. Fuoss, C. Thompson, J.A. Eastman, S.K. Streiffer, G.B. Stephenson, Polarization switching without domain formation at the intrinsic coercive field in ultrathin ferroelectric PbTiO$_3$, Phys. Rev. Lett. 105 (2010) 167601, doi:10.1103/PhysRevLett.105.167601.

[4] S. Choudhury, L.Q. Chen, Y.L. Li, Correlation between number of ferroelectric variants and coercive field of lead ziconate titanate single crystals, Appl. Phys. Lett. 91 (2007) 032902, doi:10.1063/1.2759274.

[5] P. Gao, J. Britson, J.R. Jokisaari, C.T. Nelson, S.H. Baek, Y. Wang, C.B. Eom, L.Q. Chen, X. Pan, Atomic-scale mechanisms of ferroelastic domain-wall-mediated ferroelectric switching, Nat. Commun. 4 (2013) 1–9, doi:10.1038/ncomms3791.

[6] B.W. Wessels, Ferroelectric epitaxial thin films for integrated optics, Annu. Rev. Mater. Res. 37 (2007) 659–679, doi:10.1146/annurev.matsci.37.052506.084226.

[7] S. Zhang, F. Li, X. Jiang, J. Kim, J. Luo, X. Geng, Advantages and challenges of relaxor-PbTiO$_3$ ferroelectric crystals for electroacoustic transducers-a review, Prog. Mater. Sci. 68 (2015) 1–66, doi:10.1016/j.pmatsci.2014.10.002.

[8] J.F. Scott, C.A Paz de Araujo, Ferroelectric memories, Science 246 (1989) 1400–1405 Science. doi:10.1126/science.246.4936.1400.

[9] J. Íñiguez, P. Zubko, I. Luk'yanchuk, A. Cano, Ferroelectric negative capacitance, Nat. Rev. Mater. 4 (2019) 243–256, doi:10.1038/s41578-019-0089-0.

[10] D. Li, D.A. Bonnell, Controlled patterning of ferroelectric domains: fundamental concepts and applications, Annu. Rev. Mater. Res. 38 (2008) 351–368, doi:10.1146/annurev.matsci.37.052506.084303.

[11] L. Feigl, P. Yudin, I. Stolichnov, T. Sluka, K. Shapovalov, M. Mtebwa, C.S. Sandu, X.K. Wei, A.K. Tagantsev, N. Setter, Controlled stripes of ultrafine ferroelectric domains, Nat. Commun. 5 (2014) 4677, doi:10.1038/ncomms5677.

[12] S. Li, Y.L. Zhu, Y.L. Tang, Y. Liu, S.R. Zhang, Y.J. Wang, X.L. Ma, Thickness-dependent a/a domain evolution in ferroelectric PbTiO$_3$ films, Acta Mater. 131 (2017) 123–130, doi:10.1016/j.actamat.2017.03.064.

[13] D. Chen, Z. Chen, Q. He, J.D. Clarkson, C.R. Serrao, A.K. Yadav, M.E. Nowakowski, Z. Fan, L. You, X. Gao, D. Zeng, L. Chen, A.Y. Borisevich, S. Salahuddin, J.M. Liu, J. Bokor, Interface engineering of domain structures in BiFeO$_3$ thin films, Nano Lett. 17 (2017) 486–493, doi:10.1021/acs.nanolett.6b04512.

[14] Y.H. Chu, M.P. Cruz, C.H. Yang, L.W. Martin, P.L. Yang, J.X. Zhang, K. Lee, P. Yu, L.Q. Chen, R. Ramesh, Domain control in multiferroic BiFeO$_3$ through substrate vicinality, Adv. Mater. 19 (2007) 2662–2666, doi:10.1002/adma.200602972.

[15] Z. Chen, J. Liu, Y. Qi, D. Chen, S.-L. Hsu, A.R. Damodaran, X. He, A.T. N'Diaye, A. Rockett, L.W. Martin, 180°Ferroelectric stripe nanodomains in BiFeO$_3$ thin films, Nano Lett. 15 (2015) 6506–6513, doi:10.1021/acs.nanolett.5b02031.

[16] A.L. Roytburd, J. Ouyang, A. Artemev, Polydomain structures in ferroelectric and ferroelastic epitaxial films, J. Phys. Condens. Matter. (2017) 29, doi:10.1088/1361-648X/29/16/163001.

[17] A.R. Damodaran, J.C. Agar, S. Pandya, Z. Chen, L. Dedon, R. Xu, B. Apgar, S. Saremi, L.W. Martin, New modalities of strain-control of ferroelectric thin films, J. Phys. Condens. Matter. 28 (2016) 263001.

[18] E. Langenberg, H. Paik, E.H. Smith, H.P. Nair, I. Hanke, S. Ganschow, G. Catalan, N. Domingo, D.G. Schlom, Strain-engineered ferroelastic structures in PbTiO$_3$ films and their control by electric fields, ACS Appl. Mater. Interfaces 12 (2020) 20691–20703, doi:10.1021/acsami.0c04381.

[19] S. Matzen, O. Nesterov, G. Rispens, J.A. Heuver, M. Biegalski, H.M. Christen, B. Noheda, Super switching and control of in-plane ferroelectric nanodomains in strained thin films, Nat. Commun. 5 (2014) 4415, doi:10.1038/ncomms5415.

[20] F. Borodavka, I. Gregora, A. Bartasyte, S. Margueron, V. Plausinaitiene, A. Abrutis, J. Hlinka, Ferroelectric nanodomains in epitaxial PbTiO$_3$ films grown on SmScO$_3$ and TbScO$_3$ substrates, J. Appl. Phys. 113 (2013) 187216, doi:10.1063/1.4801966.

[21] A.S. Everhardt, S. Matzen, N. Domingo, G. Catalan, B. Noheda, Ferroelectric domain structures in low-strain BaTiO$_3$, Adv. Electron. Mater. 2 (2016) 1500214, doi:10.1002/aelm.201500214.

[22] C. Tan, J. Ouyang, X. Zhong, J. Wang, M. Liao, L. Gong, C. Ren, G. Zhong, S. Zheng, H. Guo, Y. Zhou, Crystallographically engineered hierarchical polydomain nanostructures in perovskite ferroelectric films, Acta Mater. 171 (2019) 282–290, doi:10.1016/j.actamat.2019.04.029.

[23] R. Xu, S. Liu, I. Grinberg, J. Karthik, A.R. Damodaran, A.M. Rappe, L.W. Martin, Ferroelectric polarization reversal via successive ferroelastic transitions, Nat. Mater. 14 (2015) 79–86, doi:10.1038/nmat4119.

[24] M.J. Zou, Y.L. Tang, Y.L. Zhu, Y.P. Feng, Y.J. Wang, M.J. Han, N.B. Zhang, J.Y. Ma, B. Wu, X.L. Ma, Anisotropic strain: a critical role in domain evolution in (111)- oriented ferroelectric films, Acta Mater. 166 (2019) 503–511, doi:10.1016/j.actamat.2019.01.005.

[25] S.M. Yang, Y.J. Shin, Y. Ehara, H. Funakubo, J.G. Yoon, J.F. Scott, T.W. Noh, Superdomain structure and high conductivity at the vertices in the (111)-oriented epitaxial tetragonal Pb(Zr,Ti)O$_3$ thin film, Curr. Appl. Phys. 19 (2019) 418–423, doi:10.1016/j.cap.2019.01.010.

[26] P. Sharma, R.G.P. McQuaid, L.J. McGilly, J.M. Gregg, A. Gruverman, Nanoscale

dynamics of superdomain boundaries in single-crystal $BaTiO_3$ lamellae, Adv. Mater. 25 (2013) 1323–1330, doi:10.1002/adma.201203226.

[27] X. Lu, Z. Chen, Y. Cao, Y. Tang, R. Xu, S. Saremi, Z. Zhang, L. You, Y. Dong, S. Das, H. Zhang, L. Zheng, H. Wu, W. Lv, G. Xie, X. Liu, J. Li, L. Chen, L.Q. Chen, W. Cao, L.W. Martin, Mechanical-force-induced non-local collective ferroelastic switching in epitaxial lead-titanate thin films, Nat. Commun. 10 (2019) 3951, doi:10.1038/s41467-019-11825-2.

[28] Y.H. Shin, I. Grinberg, I.W. Chen, A.M. Rappe, Nucleation and growth mechanism of ferroelectric domain-wall motion, Nature 449 (2007) 881–884, doi:10.1038/nature06165.

[29] Y. Ishibashi, Y. Takagi, Note on ferroelectric domain switching, J. Phys. Soc. Jpn. 31 (1971) 506–510, doi:10.1143/JPSJ.31.506.

[30] J.F. Scott, A. Hershkovitz, Y. Ivry, H. Lu, A. Gruverman, J.M. Gregg, Superdomain dynamics in ferroelectric-ferroelastic films: switching, jamming, and relaxation, Appl. Phys. Rev. 4 (2017) 041104, doi:10.1063/1.5005994.

[31] A.S. Everhardt, S. Damerio, J.A. Zorn, S. Zhou, N. Domingo, G. Catalan, E.K.H. Salje, L.Q. Chen, B. Noheda, Periodicity-doubling cascades: direct observation in ferroelastic materials, Phys. Rev. Lett. 123 (2019) 087603, doi:10.1103/PhysRevLett.123.087603.

[32] J.F. Scott, D.M. Evans, M. Arredondo-Arechavala, R.S. Katiyar, R.G.P. McQuaid, J.M. Gregg, Nonequilibrium ferroelectric-ferroelastic 10 nm nanodomains: wrinkles, period-doubling, and power-law relaxation, J. Phys. Condens. Matter. 29 (2017) 304001, doi:10.1088/1361-648X/aa77da.

[33] G. Catalan, J. Seidel, R. Ramesh, J.F. Scott, Domain wall nanoelectronics, Rev. Mod. Phys. 84 (2012) 119–156, doi:10.1103/RevModPhys.84.119.

[34] H. Cheng, J. Ouyang, Y.X. Zhang, D. Ascienzo, Y. Li, Y.Y. Zhao, Y. Ren, Demonstration of ultra-high recyclable energy densities in domain-engineered ferroelectric films, Nat. Commun. 8 (2017), doi:10.1038/s41467-017-02040-y.

[35] A.L. Roytburd, Thermodynamics of polydomain heterostructures. I. Effect of macrostresses, J. Appl. Phys. 83 (1998) 228–238, doi:10.1063/1.366677.

[36] S.P. Alpay, A.L. Roytburd, Thermodynamics of polydomain heterostructures. III. Domain stability map, J. Appl. Phys. 83 (1998) 4714–4723, doi:10.1063/1.367260.

[37] A.L. Roytburd, Thermodynamics of polydomain heterostructures. II. Effect of microstresses, J. Appl. Phys. 83 (1998) 239–245, doi:10.1063/1.366678.

[38] Y.M. Jin, Y.U. Wang, A.G. Khachaturyan, J.F. Li, D. Viehland, Adaptive ferroelectric states in systems with low domain wall energy: tetragonal microdomains, J. Appl. Phys. 94 (2003) 3629–3640, doi:10.1063/1.1599632.

[39] Y.M. Jin, Y.U. Wang, A.G. Khachaturyan, J.F. Li, D. Viehland, Conformal miniaturization of domains with low domain-wall energy: monoclinic ferroelectric states near the morphotropic phase boundaries, Phys. Rev. Lett. 91 (2003) 197601, doi:10.1103/PhysRevLett.91.197601.

[40] D.W. Baker, P.A. Thomas, N. Zhang, A.M. Glazer, A comprehensive study of the phase diagram of $K_xNa_{1-x}NbO_3$, Appl. Phys. Lett. 95 (2009) 091903, doi:10.1063/1.3212861.

[41] L. von Helden, L. Bogula, P.E. Janolin, M. Hanke, T. Breuer, M. Schmidbauer, S. Ganschow, J. Schwarzkopf, Huge impact of compressive strain on phase transition temperatures in epitaxial ferroelectric $K_xNa_{1-x}NbO_3$ thin films, Appl. Phys. Lett. 114 (2019) 232905, doi:10.1063/1.5094405.

[42] J. Schwarzkopf, D. Braun, M. Hanke, R. Uecker, M. Schmidbauer, Strain engineering of ferroelectric domains in $K_xNa_{1-x}NbO_3$ epitaxial layers, Front. Mater. 4 (2017) 1–10, doi:10.3389/fmats.2017.00026.

[43] L. von Helden, M. Schmidbauer, S. Liang, M. Hanke, R. Wördenweber, J. Schwarzkopf, Ferroelectric monoclinic phases in strained $K_{0.70}$ $Na_{0.30}$ NbO_3 thin films promoting selective surface acoustic wave propagation, Nanotechnology 29 (2018) 415704, doi:10.1088/1361-6528/aad485.

[44] L. Bogula, L. von Helden, C. Richter, M. Hanke, J. Schwarzkopf, M. Schmidbauer, Ferroelectric phase transitions in multi-domain $K_{0.9}Na_{0.1}NbO_3$ epitaxial thin films, Nano Futur 4 (2020) 1–8, doi:10.1088/2399-1984/ab9f18.

[45] B. Wang, H.N.N. Chen, J.J.J. Wang, L.Q. Chen, Ferroelectric domain structures and temperature-misfit strain phase diagrams of $K_{1-x}Na_xNbO_3$ thin films: a phase-field study, Appl. Phys. Lett. 115 (2019) 092902, doi:10.1063/1.5116910.

[46] D. Braun, M. Schmidbauer, M. Hanke, A. Kwasniewski, J. Schwarzkopf, Tunable ferroelectric domain wall alignment in strained monoclinic $K_xNa_{1-x}NbO_3$ epitaxial films, Appl. Phys. Lett. 110 (2017) 232903, doi:10.1063/1.4985191.

[47] M. Schmidbauer, L. Bogula, B. Wang, M. Hanke, L. von Helden, A. Ladera, J.J. Wang, L.Q. Chen, J. Schwarzkopf, Temperature dependence of three-dimensional domain wall arrangement in ferroelectric $K_{0.9}$ $Na_{0.1}$ NbO_3 epitaxial thin films, J. Appl. Phys. 128 (2020) 184101, doi:10.1063/5.0029167.

[48] W. Wu, S. Bai, M. Yuan, Y. Qin, Z.L. Wang, T. Jing, Lead zirconate titanate nanowire textile nanogenerator for wearable energy-harvesting and self-powered devices, ACS Nano 6 (2012) 6231–6235, doi:10.1021/nn3016585.

[49] J.F. Li, K. Wang, F.Y. Zhu, L.Q. Cheng, F.Z. Yao, (K, Na)NbO3-based lead-free piezoceramics: fundamental aspects, processing technologies, and remaining challenges, J. Am. Ceram. Soc. 96 (2013) 3677–3696, doi:10.1111/jace.12715.

[50] X.X. Wang, J. Wu, D. Xiao, J. Zhu, X. Cheng, T. Zheng, B. Zhang, X. Lou, X.X. Wang, Giant piezoelectricity in potassium-sodium niobate lead-free ceramics, J. Am. Chem. Soc. 136 (2014) 2905–2910, doi:10.1021/ja500076h.

[51] J. Wu, D. Xiao, J. Zhu, Potassium-sodium niobate lead-free piezoelectric materials: past, present, and future of phase boundaries, Chem. Rev. 115 (2015) 2559–2595, doi:10.1021/cr5006809.

[52] S. Zhang, R. Xia, T.R. Shrout, Lead-free piezoelectric ceramics vs. PZT? J. Electroceram. 19 (2007) 251–257, doi:10.1007/s10832-007-9056-z.

[53] S.O. Leontsev, R.E. Eitel, Progress in engineering high strain lead-free piezoelectric ceramics, Sci. Technol. Adv. Mater. 11 (2010) 044302, doi:10.1088/1468-6996/11/4/044302.

[54] L. Egerton, D.M. Dillon, Piezoelectric and dielectric properties of ceramics in the system potassium-sodium niobate, J. Am. Ceram. Soc. 42 (1959) 438–442, doi:10.1111/j.1151-2916.1959.tb12971.x.

[55] Y. Saito, H. Takao, T. Tani, T. Nonoyama, K. Takatori, T. Homma, T. Nagaya, M. Nakamura, Lead-free piezoceramics, Nature 432 (2004) 84–87, doi:10.1038/nature03028.

[56] J. Rödel, W. Jo, K.T.P. Seifert, E.M. Anton, T. Granzow, D. Damjanovic, Perspective on the development of lead-free piezoceramics, J. Am. Ceram. Soc. 92 (2009) 1153–1177, doi:10.1111/j.1551-2916.2009.03061.x.

[57] N. Izyumskaya, Y.I. Alivov, S.J. Cho, H. Morkoç, H. Lee, Y.S. Kang, Processing, structure, properties, and applications of PZT thin films, Crit. Rev. Solid State Mater. Sci. 32 (2007) 111–202, doi:10.1080/10408430701707347.

[58] M. Schmidbauer, D. Braun, T. Markurt, M. Hanke, J. Schwarzkopf, Strain engineering of monoclinic domains in $K_xNa_{1-x}NbO_3$ epitaxial layers: a pathway to enhanced piezoelectric properties, Nanotechnology 28 (2017) 24LT02, doi:10.1088/1361-6528/aa715a.

[59] J. Luo, W. Sun, Z. Zhou, H.Y. Lee, K. Wang, F. Zhu, Y. Bai, Z.J. Wang, J.F. Li, Monoclinic (K,Na)NbO_3 ferroelectric phase in epitaxial films, Adv. Electron. Mater. 3 (2017) 1700226, doi:10.1002/aelm.201700226.

[60] K.N. Pham, N.H. Gaukås, M. Morozov, T. Tybell, P.E. Vullum, T. Grande, M.A. Einarsrud, Epitaxial $K_{0.5}Na_{0.5}NbO_3$ thin films by aqueous chemical solution deposition, R. Soc. Open Sci. 6 (2019) 180989, doi:10.1098/rsos.180989.

[61] Q. Yu, J.F. Li, W. Sun, Z. Zhou, Y. Xu, Z.K. Xie, F.P. Lai, Q.M. Wang, Electrical properties of $K_{0.5}$ $Na_{0.5}$ NbO_3 thin films grown on Nb:$SrTiO_3$ single-crystalline substrates with different crystallographic orientations, J. Appl. Phys. 113 (2013) 024101, doi:10.1063/1.4773542.

[62] K. Shibata, K. Suenaga, A. Nomoto, T. Mishima, Curie Temperature, Biaxial elastic modulus, and thermal expansion coefficient of (K,Na)NbO_3 piezoelectric thin films, Jpn. J. Appl. Phys. 48 (2009) 121408, doi:10.1143/JJAP.48.121408.

[63] K. Shibata, F. Oka, A. Ohishi, T. Mishima, I. Kanno, Piezoelectric properties of (K,Na)NbO_3 films deposited by RF magnetron sputtering, Appl. Phys. Express 1 (2008) 011501, doi:10.1143/APEX.1.011501.

[64] S. Zhang, Z. Zhou, J. Luo, J. Li, Potassium-sodium-niobate-based thin films: lead free for micro-piezoelectrics, Ann. Phys. 531 (2019) 1800525, doi:10.1002/andp.201800525.

[65] J. Luo, S. Zhang, Z. Zhou, Y. Zhang, H. Lee, Z. Yue, J. Li, Phase transition and piezoelectricity of $BaZrO_3$ -modified (K,Na)NbO_3 lead-free piezoelectric thin films, J. Am. Ceram. Soc. 102 (2018) jace.16172, doi:10.1111/jace.16172.

[66] L. Hao, Y. Yang, Y. Huan, H. Cheng, Y.Y. Zhao, Y. Wang, J. Yan, W. Ren, J. Ouyang, Achieving a high dielectric tunability in strain-engineered tetragonal $K_{0.5}Na_{0.5}NbO_3$ films, Npj Comput. Mater. 7 (2021) 62, doi:10.1038/s41524-021-00528-2.

[67] M.J. Zhou, J.J. Wang, L.Q. Chen, C.W. Nan, Strain, temperature, and electric-field effects on the phase transition and piezoelectric responses of $K_{0.5}$ $Na_{0.5}$ NbO_3 thin films, J. Appl. Phys. 123 (2018) 154106, doi:10.1063/1.5027505.

[68] G. Bai, W. Ma, Phenomenological analysis of phase transitions in epitaxial perovskite ferroelectric thin films, Phys. B Condens. Matter. 405 (2010) 1901–1907, doi:10.1016/j.physb.2010.01.070.

[69] B. Wang, L. Bogula, Adriana Ladera, M.J. Zhou, J.J. Wang, L.Q. Chen, unpublised.

[70] Y.L. Li, S.Y. Hu, Z.K. Liu, L.Q. Chen, Effect of substrate constraint on the stability and evolution of ferroelectric domain structures in thin films, Acta Mater. 50 (2002) 395–411, doi:10.1016/S1359-6454(01)00360-3.

[71] J.J. Wang, B. Wang, L.Q. Chen, Understanding, predicting, and designing ferroelectric domain structures and switching guided by the phase-field method, Annu. Rev. Mater. Res. 49 (2019) 127–152, doi:10.1146/annurev-matsci-070218-121843.

[72] L.Q. Chen, Phase-field method of phase transitions/domain structures in ferroelectric thin films: a review, J. Am. Ceram. Soc. 91 (2008) 1835–1844, doi:10.1111/j.1551-2916.2008.02413.x.

[73] M.J. Zhou, T. Yang, J.J. Wang, Z. Ren, L.Q. Chen, C.W. Nan, Nanopore-induced dielectric and piezoelectric enhancement in $PbTiO_3$ nanowires, Acta Mater. 187 (2020) 146–152, doi:10.1016/j.actamat.2020.01.023.

[74] http://mupro.co, (n.d.).

[75] Y.L. Li, S.Y. Hu, Z.K. Liu, L.Q. Chen, Effect of electrical boundary conditions on ferroelectric domain structures in thin films, Appl. Phys. Lett. 81 (2002) 427–429, doi:10.1063/1.1492025.

[76] P.E. Janolin, Strain on ferroelectric thin films, J. Mater. Sci. 44 (2009) 5025–5048, doi:10.1007/s10853-009-3553-1.

[77] G. Sheng, J.X. Zhang, Y.L. Li, S. Choudhury, Q.X. Jia, Z.K. Liu, L.Q. Chen, Misfit strain–misfit strain diagram of epitaxial $BaTiO_3$ thin films: thermodynamic calculations and phase-field simulations, Appl. Phys. Lett. 93 (2008) 232904, doi:10.1063/1.3039410.

[78] G. Sheng, J.X. Zhang, Y.L. Li, S. Choudhury, Q.X. Jia, Z.K. Liu, L.Q. Chen, Domain stability of $PbTiO_3$ thin films under anisotropic misfit strains: phase-field simulations, J. Appl. Phys. 104 (2008) 054105, doi:10.1063/1.2974093.

[79] S. Kobayashi, K. Inoue, T. Kato, Y. Ikuhara, T. Yamamoto, Multiphase nanodomains in a strained $BaTiO_3$ film on a $GdScO_3$ substrate, J. Appl. Phys. 123 (2018) 064102, doi:10.1063/1.5012545.

[80] A.S. Everhardt, T. Denneulin, A. Grünebohm, Y.T. Shao, P. Ondrejkovic, S. Zhou, N. Domingo, G. Catalan, J. Hlinka, J.M. Zuo, S. Matzen, B. Noheda, Temperature-independent giant dielectric response in transitional $BaTiO_3$ thin films, Appl. Phys. Rev. 7 (2020) 011402, doi:10.1063/1.5122954.

[81] W. Peng, J.A. Zorn, J. Mun, M. Sheeraz, C.J. Roh, J. Pan, B. Wang, K. Guo, C.W. Ahn, Y. Zhang, K. Yao, J.S. Lee, J. Chung, T.H. Kim, L. Chen, M. Kim, L. Wang, T.W. Noh, Constructing polymorphic nanodomains in $BaTiO_3$ films via epitaxial symmetry engineering, Adv. Funct. Mater. 30 (2020) 1910569, doi:10.1002/adfm.201910569.

[82] H. Pohlmann, J.-J. Wang, B. Wang, L.-Q. Chen, A thermodynamic potential and the temperature-composition phase diagram for single-crystalline $K_{1-x}Na_xNbO_3$ ($0 \leq x \leq 0.5$), Appl. Phys. Lett. 110 (2017) 102906, doi:10.1063/1.4978360.

[83] D.J. Srolovitz, J.F. Scott, Clock-model description of incommensurate ferroelectric films and of nematic-liquid-crystal films, Phys. Rev. B 34 (1986) 1815–1819, doi:10.1103/PhysRevB.34.1815.

[84] J.F. Scott, A. Schilling, S.E. Rowley, J.M. Gregg, Some current problems in perovskite nano-ferroelectrics and multiferroics: kinetically-limited systems of finite lateral size, Sci. Technol. Adv. Mater. 16 (2015) 036001, doi:10.1088/1468-6996/16/3/036001.

[85] E.K.H. Salje, O. Aktas, M.A. Carpenter, V.V. Laguta, J.F. Scott, Domains within domains and walls within walls: evidence for polar domains in cryogenic $SrTiO_3$, Phys. Rev. Lett. 111 (2013) 247603, doi:10.1103/PhysRevLett.111.247603.

[86] G. Catalan, H. Béa, S. Fusil, M. Bibes, P. Paruch, A. Barthélémy, J.F. Scott, Fractal dimension and size scaling of domains in thin films of multiferroic $BiFeO_3$, Phys. Rev. Lett. 100 (2008) 027602, doi:10.1103/PhysRevLett.100.027602.

[87] T. Tybell, P. Paruch, T. Giamarchi, J.M. Triscone, Domain wall creep in epitaxial ferroelectric $Pb(Zr_{0.2}Ti_{0.8})O_3$ Thin Films, Phys. Rev. Lett. 89 (2002) 097601, doi:10.1103/PhysRevLett.89.097601.

[88] W. Cao, L.E. Cross, Theory of tetragonal twin structures in ferroelectric perovskites with a first-order phase transition, Phys. Rev. B 44 (1991) 5–12, doi:10.1103/PhysRevB.44.5.

[89] J. Hlinka, P. Márton, Phenomenological model of a 90° domain wall in $BaTiO_3$-type ferroelectrics, Phys. Rev. B 74 (2006) 104104, doi:10.1103/PhysRevB.74.104104.

[90] J.W. Cahn, J.E. Hilliard, Free energy of a nonuniform system. I. Interfacial free energy, J. Chem. Phys. 28 (1958) 258–267, doi:10.1063/1.1744102.

[91] B. Meyer, D. Vanderbilt, Ab initio study of ferroelectric domain walls in $PbTiO_3$, Phys. Rev. B 65 (2002) 104111, doi:10.1103/PhysRevB.65.104111.

[92] J. Seidel, D. Fu, S.Y. Yang, E. Alarcón-Lladó, J. Wu, R. Ramesh, J.W. Ager, Efficient photovoltaic current generation at ferroelectric domain walls, Phys. Rev. Lett. 107 (2011) 126805, doi:10.1103/PhysRevLett.107.126805.

[93] P.V. Yudin, M.Y. Gureev, T. Sluka, A.K. Tagantsev, N. Setter, Anomalously thick domain walls in ferroelectrics, Phys. Rev. B. 91 (2015) 060102, doi:10.1103/PhysRevB.91.060102.

[94] J. Seidel, L.W. Martin, Q. He, Q. Zhan, Y.H. Chu, A. Rother, M.E. Hawkridge, P. Maksymovych, P. Yu, M. Gajek, N. Balke, S.V. Kalinin, S. Gemming, F. Wang, G. Catalan, J.F. Scott, N.A. Spaldin, J. Orenstein, R. Ramesh, Conduction at domain walls in oxide multiferroics, Nat. Mater. 8 (2009) 229–234, doi:10.1038/nmat2373.

[95] R. Xu, J. Karthik, A.R. Damodaran, L.W. Martin, Stationary domain wall contribution to enhanced ferroelectric susceptibility, Nat. Commun. 5 (2014) 3120, doi:10.1038/ncomms4120.

[96] H. Lu, Y. Tan, J.P.V. McConville, Z. Ahmadi, B. Wang, M. Conroy, K. Moore, U. Bangert, J.E. Shield, L. Chen, J.M. Gregg, A. Gruverman, Electrical tunability of domain wall conductivity in $LiNbO_3$ thin films, Adv. Mater. 31 (2019) 1902890, doi:10.1002/adma.201902890.

[97] A.Q. Jiang, Y. Zhang, Next-generation ferroelectric domain-wall memories: principle and architecture, NPG Asia Mater. 11 (2019) 2, doi:10.1038/s41427-018-0102-x.

[98] J. Fousek, V. Janovec, The orientation of domain walls in twinned ferroelectric crystals, J. Appl. Phys. 40 (1969) 135–142, doi:10.1063/1.1657018.

[99] J. Sapriel, Domain-wall orientations in ferroelastics, Phys. Rev. B 12 (1975) 5128–5140, doi:10.1103/PhysRevB.12.5128.

[100] A.G. Khachaturyan, Theory of Structural Transformations in Solids, Wiley, New York, 1983.

[101] J.M. Ball, Convexity conditions and existence theorems in nonlinear elasticity, Arch. Ration. Mech. Anal. 63 (1976) 337–403, doi:10.1007/BF00279992.

[102] J.M. Ball, D.R. James, Proposed experimental tests of a theory of fine microstructure and the two-well problem, Philos. Trans. R. Soc. Math. Phys. Eng. Sci. 338 (1992) 389–450, doi:10.1098/rsta.1992.0013.

[103] R.J. Harrison, S.A.T. Redfern, A. Buckley, E.K.H. Salje, Application of real-time, stroboscopic X-ray diffraction with dynamical mechanical analysis to characterize the motion of ferroelastic domain walls, J. Appl. Phys. 95 (2004) 1706–1717, doi:10.1063/1.1639949.

[104] S. Kustov, I. Liubimova, E.K.H. Salje, Domain dynamics in quantum-paraelectric $SrTiO_3$, Phys. Rev. Lett. 124 (2020) 016801, doi:10.1103/PhysRevLett.124.016801.

[105] B. Casals, G.F. Nataf, E.K.H. Salje, Avalanche criticality during ferroelectric/ferroelastic switching, Nat. Commun. 12 (2021) 1–7, doi:10.1038/s41467-020-20477-6.